Sensors and Actuators B 243 (2017) 990–1001

Contents lists available at ScienceDirect

Sensors and Actuators B: Chemical

journal homepage: www.elsevier.com/locate/snb

# Au Decorated ZnO hierarchical architectures: Facile synthesis, tunable morphology and enhanced CO detection at room temperature

S. Arunkumar, Tianfeng Hou, Young-Bae Kim, Byungchul Choi, Su Han Park, Seunghun Jung, Dong-Weon Lee *

*School of Mechanical Systems Engineering, Chonnam National University, Gwangju-61186, Republic of Korea*

ARTICLE INFO

*Article history:*
Received 16 July 2016
Received in revised form 29 October 2016
Accepted 27 November 2016
Available online 30 November 2016

*Keywords:*
Zinc oxide nanostructures
Gold nanoparticles
Carbon monoxide sensor
Room temperature CO sensing

ABSTRACT

A highly selective and sensitive gas sensing material was prepared by decorating gold (Au) nanoparticles on zinc oxide *(ZnO)* nanostructure. First, zinc oxide architectures were synthesised through facile one-pot hydrothermal synthesis route by using zinc acetate as the metal precursors, ethanolamine as the organic Lewis base and water as the reaction medium. The versatile zinc oxide architectures such as (i) nanostars *(ZNS)*, (ii) marigold flower *(ZMF)*, (iii) nanorods assembled flower *(ZNF)* and (iv) nanorods *(ZNR)* were successfully synthesised by the controlled variation of the reaction medium mole ratio. The crystal structure and morphological evaluation of the as prepared material were investigated in detail by several analytical techniques, and the findings are consistent with each other. The carbon monoxide (CO) sensing ability of the as prepared materials was carried out at different sensing temperature ($Ts \leq 300\,^{\circ}C$) and at different gas concentration (5–1000 *ppm*). Gas sensing study clearly shows that the sensor responses are found to be morphology and surface area dependent. Among all the zinc oxide nanostructures, nanostars exhibits excellent sensitivity ($S_R \sim 31$ toward 5 *ppm*) at the optimized sensing temperature of 275 °C. Further, to improve the sensing characteristics and to reduce the operating temperature, different wt% of gold nanopartilces were decorated on the surface of zinc oxide nano-stars by solution impregnation technique. Surface decoration of only 3 wt% gold nanoparticles incorporated zinc oxide nanostars exhibits enhanced sensing response ($S_R \sim 15$ toward 50 *ppm*) at 35 °C with an excellent response ($\Gamma_{RES} \sim 8$ s) and recovery ($\Gamma_{REC} \sim 15$ s) time. Sensor also posses excellent selectivity toward CO compare to other interfering gases such as methanol, ethanol, acetone and hydrogen.



**Contents**

1. Introduction ..... 991
2. Experimental detail ..... 991
   2.1. Chemicals ..... 991
   2.2. Preparation of ZnO nano-stars ..... 991
   2.3. Incorporation of gold nanoparticles ..... 992
   2.4. Gas sensor fabrication and measurements ..... 992
3. Details of experimental methods and characterization techniques ..... 992
4. Results and discussions ..... 992
   4.1. Morphological and crystal structure evaluations ..... 992
   4.2. Effect of ethanolamine ..... 993
5. Gas sensing characteristics ..... 995
6. Generalised sensing mechanism ..... 997
7. Proposed sensing mechanism based on FTIR analysis ..... 999
8. Conclusion ..... 999

* Corresponding author. Tel.: +82 62 530 1684.
*E-mail address:* mems@jnu.ac.kr (D.-W. Lee).

http://dx.doi.org/10.1016/j.snb.2016.11.152
0925-4005/

Acknowledgements ..... 999
Appendix A. Supplementary data ..... 999
References ..... 999
Biographies ..... 1001

## 1. Introduction

Air pollutants released from the automotives and industries cause major concerns to human safety and environmental issues. Among all air pollutants, carbon monoxide (CO) is one of the most harmful pollutants which reacts readily with haemoglobin and damages the human body by causing a reduction in cellular respiration. A trace amount of carbon monoxide (TLV ~50 *ppm*) inhalation causes large number of deaths annually in the world [1–4]. Therefore, the development of sensor for selective and sensitive detection of CO with a faster response at ambient temperature is highly desired.

Over the years, several solid state gas sensors have been developed to detect CO but most of the commercial sensors available in the market, work at relatively high temperature. The disadvantage of the higher operating temperature sensor is the less long term durability due to a thermally induced growth of metal oxide grains. The other problem associated with those sensors is the sensor fabrication costs and power consumption. Hence developing the ambient temperature sensor system is very important as it provides very low power consumption. More importantly we can simplify the device fabrication by eliminating the heater component and reduces the operating cost [5]. This major bottleneck calls for worldwide research effort in the areas of design and development of novel materials, their complete characterization, sensor fabrication, calibration and testing of the sensor device. This has been achieved by several years of research on metal-oxide based gas sensors that has provided key understanding on the control parameters and processes for materials engineering. Over the years, quite a few strategies have been employed to reduce the working temperature. Some of the most popular approaches are morphological control [6], metal oxide composites [7] doping [8], carbon/graphene based nanostructured materials [9,10], incorporation of metal nanoparticles [11], ultra violet light illumination [12], micro electro mechanical system fabrication [13], etc.

Chemical gas sensing based on metal oxide semiconductors ($SnO_2$, $In_2O_3$, ZnO, $Fe_2O_3$, $WO_3$, etc.) have been considered as one of the most important technological developments for the pollution monitoring, environmental sustainability, and personal healthcare [14–18]. Among these metal oxide semiconductors, zinc oxide has received great attention for the detection of various toxic/hazardous gases owing to their excellent physico-chemical, opto-electronic properties, high mobility of conduction electrons, thermal stability, high response, long term stability and recyclability [19–25]. In spite of all these interesting advances, the usage of zinc oxide based gas sensor has met limited success due to their higher operating temperature and lower selectivity.

Since the gas sensing kinetics reactions occurring on the metal oxide surface, several intensive efforts have been made to improve the gas sensing characteristics of zinc oxide by engineering their structure, size, morphology, surface and porosity to suit the materials for better sensor performance. For example Zhang et al. successfully prepared zinc oxide hollow nanofiberes and evaluated its ethanol gas sensing properties at 280 °C, which exhibited excellent sensing properties due to their special one-dimensional nanostructural properties [26]. Tian et al. demonstrated in detail the role of zinc oxide surface structure for the enhanced benzene sensing performances of zinc oxide nanorods at 320 °C [27]. Yin et al. reported the successful formation of zinc oxide hollow spheres and demonstrated that they could perform well as the efficient alcohol sensor at 300 °C [28]. Over the years, several strategies demonstrated that the incorporation metal nanoparticles such as Au, Pt, Pd, and Ag to the metal oxides surface can effectively reduce the operating temperature and improve the lower limit detection, sensor response, sensitivity, and selectivity [29–33]. Many studies have established that the gold nanopartilces can be effectively used for the CO oxidation at low temperature. For instance, Joshi et al. demonstrated the enhanced catalytic and the chemical sensitization effect of Au nanoparticles towards CO through Au decorated zinc oxide nanowires and they could successfully detect carbon monoxide at room temperature [34].

In continuation of these great efforts here we have developed a highly effective and efficient room temperature carbon monoxide sensor one-pot hydrothermal synthesis route. The versatile zinc oxide nanostructures include (i) nano-stars, (ii) marigold flower, (iii) nanorods assembled flowers and (iv) nanorods were successfully prepared by the controlled variation of $Zn^{2+}$/ethanolamine mole ratio. The as prepared materials were characterised extensively by different analytical techniques. Morphological evaluations of the as prepared materials were carried out by field emission scanning electron microscopy and transmission electron microscopy along with selected area electron diffraction analysis. The CO gas sensing properties of as prepared zinc oxide nanostructures were also evaluated at different sensing temperatures ($T_s$) ≤ 300 °C towards different gas concentrations ranging from 1000 to 5 *ppm*. The as prepared zinc oxide nanostructures showed the enhanced sensitivity, and reasonably fast response/recovery time. Among other zinc oxide nanostructures, nanostars possess enhanced sensing behaviour in terms of higher sensor response, sensitivity ($S_R = R_a/R_g$ ~31), with fast response ($\Gamma_{RES}$ ~12 s)/recovery time ($\Gamma_{REC}$ ~11 s) toward 5 *ppm* of CO at 275 °C. In order to improve the sensitivity, selectivity and to reducing the working temperature, different wt% gold (Au) nanoparticles were incorporated into the zinc oxide nanostars by solution impregnation technique. By loading of only 3 wt% Au nanoparticles we are able to sense CO as low as 35 °C. Sensor also shows the excellent selectivity towards CO compare to other interfering gases such as methanol, ethanol, acetone, and hydrogen. To show the enhanced performance of our device we have also compared the sensing performance of our device with various semiconductor metal oxides based gas sensor toward CO (Table 1).

## 2. Experimental detail

### 2.1. Chemicals

Zinc acetate dehydrate ($Zn(CH_3COO)_2 \cdot 2H_2O$), gold chloride ($HAuCl_3$), sodium borohydride ($NaBH_4$) and ethanolamine ($NH_2CH_2CH_2OH$) were purchased from Sigma-Aldrich. All the chemicals are analytical reagent (AR) grade and used without any further purification. Deionised water was used throughout the experiment.

### 2.2. Preparation of ZnO nano-stars

The hierarchical zinc oxide architectures were prepared by the following the literature method with some modifications [35]. In a typical synthesis procedure 2 mmol of zinc acetate dehydrate

**Table 1**
Comparison of sensing performances of our proposed CO sensor with other published CO sensors based on metal oxide composites.

| Material | $T_s$ (°C) | $S_R$ | $G_C$ | $\Gamma_{RES}$ | $\Gamma_{REC}$ | Ref |
|---|---|---|---|---|---|---|
| Al-doped ZnO nanoparticles. | 300 | 80 | 50 ppm | 6–8 s | 16–30 s | [69] |
| $SnO_2$ nanoparticles | 300 °C | 6.4 | 3000 ppm | 2.6 s | 3.6 s | [70] |
| Tin Oxide Mixed Cerium Oxide Thin Films | 430 °C | 190 | 500 ppm | 26 s | 30 s | [71] |
| SnO2-SBA-15 | 250 | 312 | 1000 | 5 (min) | 40 (min) | [72] |
| ZnO thin film | 300 | 23 | 10–1660 | 56 (s) | 67 (s) | [73] |
| Cu-doped ZnO | 300 | 50 | 68 | 15 (s) | N/A | [74] |
| CuO NWs | 300 | 30 | ~0.07 | N/A | N/A | [75] |
| Pt-In2O3; Pd-In2O3 | R/T | 50 | ~2.8 ~7.2 | 50 (s) | 60 (s) | [76] |
| PdO nanoflake thin films | 100 °C, | 1.5 | 4000 ppm | N/A | N/A | [77] |
| Gold-Nanoparticle-Functionalized $In_2O_3$ Nanowires | RT | 104 | 200ppb–5 ppm | 130 s/ | 50 s | [78] |
| $Co_3O_4$/PEI–CNTs | RT | 30.3 | 5~1000 ppm | 8 s/ | 30 s | [79] |
| CNT/Au/$SnO_2$nanotubes | RT | 70 | 500~2500 ppm | Less than 20 s | N/A | [80] |
| Au/ZnO nanowires | RT | 5 | 100 ppm | N/A | N/A | [34] |
| ZnO Nanostars | 275 | 681 | 5 ppm–1000 ppm | 21 s | 12 s | This work |
| ZnO/Au Nanostars | RT | 55.3 | 500 ppm –50 ppm | 41 s –10 s | 40 s–12 s | This work |

N/A: Not available.

was dissolved in 30 mL of water under vigorous magnetic stirring, followed by drop by drop addition of 20 mmol of ethanolamine. After 15 min stirring the solution was transferred to the Teflon lined stainless steel autoclave and kept at 150 °C for 12 h in a programmable oven at the heating rate of 10 °C/min. After the reaction time the Teflon autoclave was oven cooled. The product was collected and washed several times with deionised water and ethanol to remove the residual impurities. Finally the product was dried at 80 °C before carrying out further characterizations. Other interesting zinc oxide architectures were prepared by the similar protocol except varying the $Zn^{2+}$/ethanolamine mole ratio. All these details are explained in detail in the following sections.

### 2.3. Incorporation of gold nanoparticles

The zinc oxide nanostructures were synthesized through the method described in the preceding section. To incorporate different weight percentages of gold nanoparticles, a solution impregnation technique was employed. The required amount of gold chloride salt was added to the as synthesized powder suspended in an aqueous medium under the constant magnetic stirring and then ultrasonically treated for 15 min. Thereafter, calculated amount sodium borohydride was added to the solution to reduce the gold chloride salt to metallic gold, Au(0), in situ. After stirring for 3 h, the precipitate was centrifuged and washed with deionized water and ethanol to remove the residual sodium borohydride and then dried at 80 °C for overnight.

### 2.4. Gas sensor fabrication and measurements

The fabrication techniques and sensor characteristics measurement setup were described in detail in our previous work [36]. For device fabrication, the as prepared zinc oxide nano structures were made into a thick homogeneous paste. The paste was coated on a cylindrical ceramic tube on which a pair of Au electrodes provided for electrical contacts. The coated substrate was mounted along with a Ni–Cr coil inserted through the ceramic tube that functions as a heater. The control on operating temperature was achieved and monitored using a PDI controller equipped with a Chromel-Alumel K-type thermocouple positioned in close proximity with the gas sensor surface. A standard resistor connected in series with the sensing element served as reference to form a complete measurement circuit. Prior to each experimentation the sensing element was pre-heated at 150 °C for 3 h in air to stabilize the sensor surface. The gas sensing capabilities of the synthesized nanostructures were thus carried out in a dry air environment from room temperature to 300 °C. All gas sensing experiments were carried out at a gas flow rate of 100 $cm^3$/min. Gas dilution to achieve the required concentration was attained by mixing requisite volume of CO with clean dry nitrogen gas. The gas sensing measurements were carried out by monitoring the changes in resistance under a constant applied voltage during cyclic exposure to different gas concentrations.

## 3. Details of experimental methods and characterization techniques

The morphological evaluations of the as prepared products were analysed by the field emission-scanning electron microscopy (JEOL JSM-7500F), Energy dispersive X-ray analysis (EDAX) performed with OXFORD Inca detector interfaced at 15 kV without sample sputtering, and transmission electron microscopy (TEM, HR-TEM, JEM-2100F, JEOL). The crystal structure identified by powder X-ray diffraction (XRD) measurements were carried out on X −Pert-pro using CuKα (λ = 0.15406 nm) radiation over a 2θ range of 2–70°. The Raman spectroscopy was performed using a NRS-5100, JASCO spectrometer. The X-ray photoelectron spectroscopy studies were carried out using a XPS, ESCALAB-MKII with AlKα X-ray (hν = 1486.6 eV) as the emission source. UV-DRS analysis was carried out on a GBC Varian UV/Vis spectrometer with KBr-diluted pellets of solid samples and pure KBr as the reference. The specific area was determined by the surface area and pore size distribution measurements using a BET (Micromeritics (ASAP2010)), surface area and pore size analyser at liquid nitrogen temperature.

## 4. Results and discussions

### 4.1. Morphological and crystal structure evaluations

The morphological evaluations of the as prepared zinc oxide nanostructured materials were characterised by electron microscopy in both scanning and transmission mode along with the selected area electron diffraction analysis and high resolution transmission electron microscopy. Fig. 1 shows the electron micrograph of the as synthesised zinc oxide architecture obtained through 1:20 mol ratio of $Zn^{2+}$/EA in 30 mL of water at 150 °C. The panoramic view (Fig. 1$a_1$) discloses the numerous nearly uniform size and shape zinc oxide with star like architecture of size ~1 to 2 μm. The higher magnification (Fig. 1$a_2$) clearly shows, each star is the building blocks of several spindle like architecture which are radiating from the centre core. Closer inspection of the spindles evidently illustrates that the each spindle is composed of numerous primary nanoparticles of size ~20 nm. The analysis clearly demonstrates the remarkable self-assembly of ultrafine nanoparticles (primary structure) to form secondary structures (spindles) which

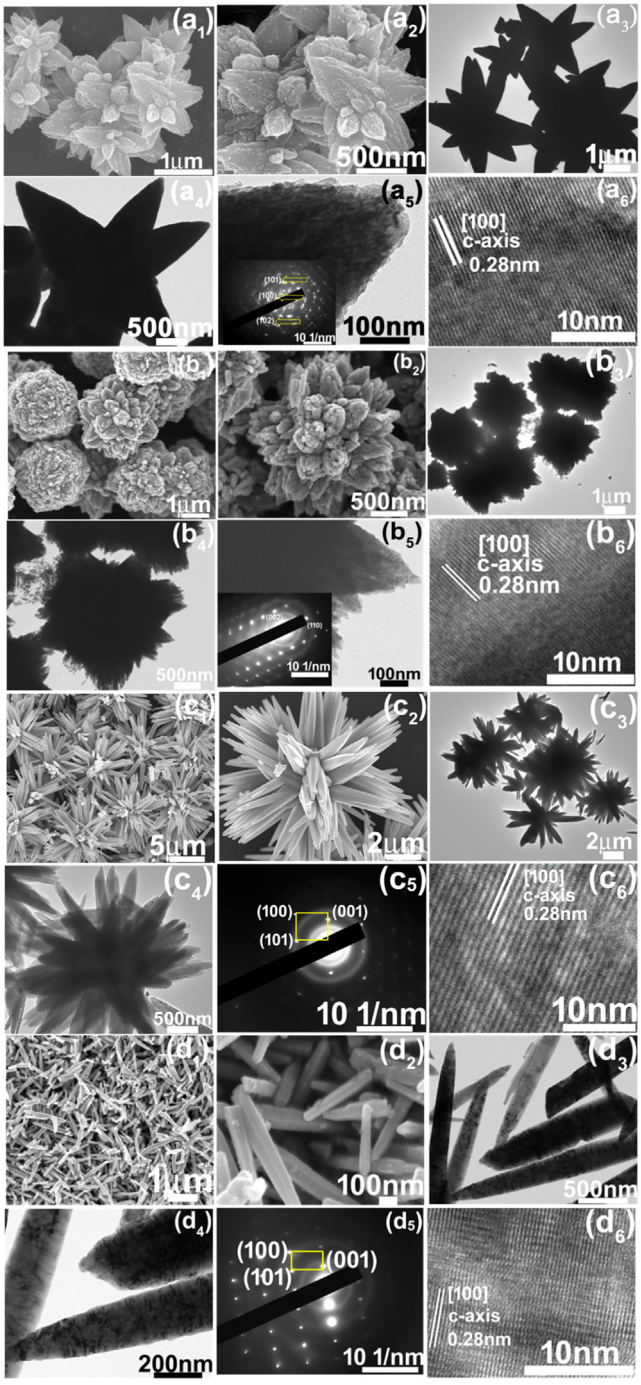


**Fig. 1.** (a-d) Electron microscopic images of as prepared zinc oxide nanostructures in scanning and transmission mode. Morphological evaluations of the as prepared zinc oxide nanostructures obtained at 150 °C with different $Zn^{2+}$/ethanolamine mole ratio. (a) nanostars, (b) marigold flower, (c), nano-rods assembled flowers and (d) nano rods.

reorganize perpendicular to the centre core to finally yield star like architecture (primary structure). The TEM analyses (Fig. 1($a_3$&$a_4$)) concur, well with the FE-SEM findings. The contrast based electron dense and electron poor region indicating the porous nature of the materials. The SAED pattern (Fig. 1$a_5$) shows well defined Laue spots specifying the high crystalline nature of the materials. The diffraction rings indicates the poly crystalline nature of the material with wurtzite crystal structure. The high resolution TEM (Fig. 1$a_6$) shows clear two-dimensional lattice fringes, which further confirms the nanostars are well crystalline. The observed lattice with a distance of 0.28 nm corresponds to the {100} lattice spacing of wurtzite zinc oxide.

### 4.2. Effect of ethanolamine

The imperative role of ethanolamine on the nucleation and growth of zinc oxide architectures were studied in detail by varying the $Zn^{2+}$ to ethanolamine mole ratio from 1:20 to 1:100 while maintaining other reaction parameter constant. The FE-SEM and TEM analysis (Fig. 1($b_1$–$d_6$)) clearly reveals that the controlled variation of $Zn^{2+}$ to ethanolamine facilitate the morphological variation of zinc oxide nanostructures. Hierarchical mesoporous marigold like flower architecture was obtained when the $Zn^{2+}$/ethanolamine mole ratio in 1:40. Fig. 1($b_1$–$b_2$) shows the FE-SEM images of the as prepared zinc oxide marigold like flower at lower and higher magnification and Fig. 1($b_3$) shows the corresponding TEM image. The electron microscopy images clearly show the porous nature of the product and closer inspection reveals that the nanoparticles of size ~10 nm are the building blocks (primary structure) for the marigold like flower. Nanorods assembled flower like architectures were obtained when the $Zn^{2+}$/ethanolamine ratio in 1:60 (Fig. 1($c_1$–$c_6$)). Nanorods (Fig. 1($d_1$–$d_6$)) of size ~100 nm were obtained with further increasing the $Zn^{2+}$/ethanolamine concentration (1: < <100). Although, the obtained morphologies are very appealing this findings need further detailed investigations to demonstrate the plausible formation mechanism of these interesting morphological evaluations.

Fig. 2(a, b) shows the TEM images of 3 wt% gold nanoparticles incorporated zinc oxide nanostars at different magnifications. The presence of the gold nanoparticles of size explicable from the higher magnified TEM image (Fig. 2(b) marked region and Fig. 2(c)). The average size distribution of the gold nanoparticles is found to be ~5–6 nm (Fig. S1). The high resolution TEM (Fig. 2(d)) shows the lattice fringes corresponding to Au and ZnO. Further, the elemental mapping (Fig. 2(e)) analysis was carried out to confirm the existence of gold nanoparticles on the surface of zinc oxide nanostars and the obtained result clearly reveals the presence of Zn, O and Au. The elemental analysis was performed comparatively in order to examine the composition of Au and ZnO.

Powder X-ray diffraction analysis was used to elucidate the crystal structures, phase purity and composition of the as-synthesized products. Fig. 3A shows the X-ray diffraction pattern of as-prepared zinc oxide nanostructures. All the diffraction patterns can be perfectly indexed to the hexagonal wurtzite crystal structured zinc oxide and the calculated lattice parameters (a = b = 3.24 A° and c = 5.20 A°) are exactly matches well with the reported values (JCPDS card no. 36–1451) [37,38]. The sharp and strong diffraction pattern indicates the high crystalline nature of the as prepared material. The well resolved Bragg's diffraction (Fig. 3B) at 38.2°, 44.5° and 64.6° can be assigned to the cubic crystal structured gold (Au) planes of (111), (200), and (220) (JCPDS no. 4–784) [39,40]. The remaining diffraction patterns are corresponding to the wurtzite structure of zinc oxide which confirms the successful formation of zinc oxide/Au composites. No other crystalline phase corresponding to any impurity was detected, indicating the high purity of the synthesised product.

Micro-Raman spectroscopy analysis were carried out to further examine the phase purity and crystal structure of the as prepared zinc oxide nanostructures. The observed optical phonon modes at 330 $cm^{-1}$, 383 $cm^{-1}$, 437 $cm^{-1}$, 574 $cm^{-1}$ (Fig. 4) are corresponds to the wurtzite crystal structure of zinc oxide which is in good agreement with the XRD analysis [41–43]. The sharp and strong intense peek at 437 $cm^{-1}$ corresponds to the fundamental optical $E_2$ (high) mode. Raman band at 383 $cm^{-1}$ arises due to the first order Raman scattering corresponding to $A_1$ (TO) phonon mode. The peak at 330 $cm^{-1}$ has been assigned by the second order or multiple-

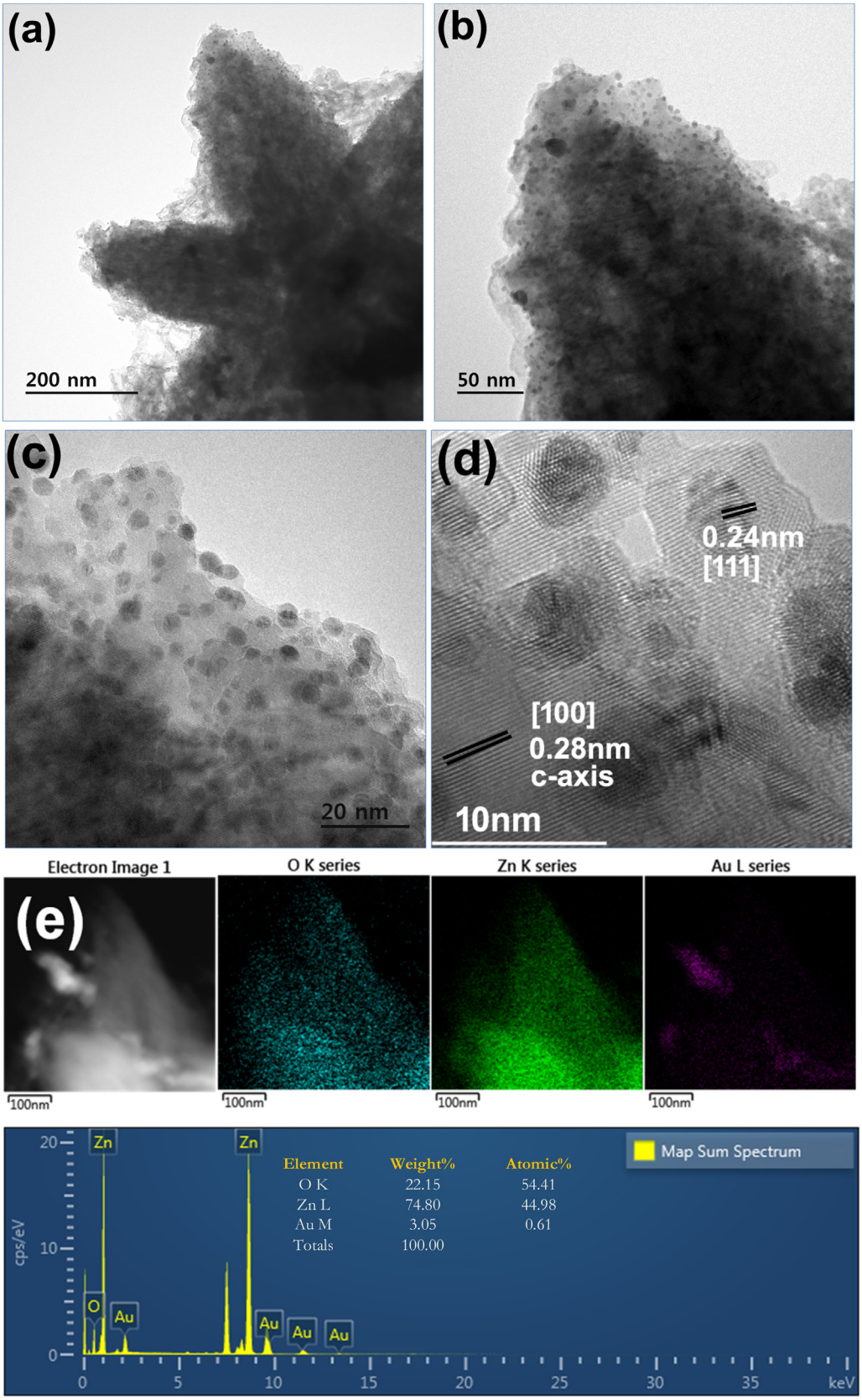


**Fig. 2.** (a-b) Transmission electron microscopy images of as prepared Au nanoparticles incorporated zinc oxide nanostars at lower and higher magnifications, (c) elemental mapping and corresponding energy dispersive spectrum indicating the presence of gold in zinc oxide matrix.

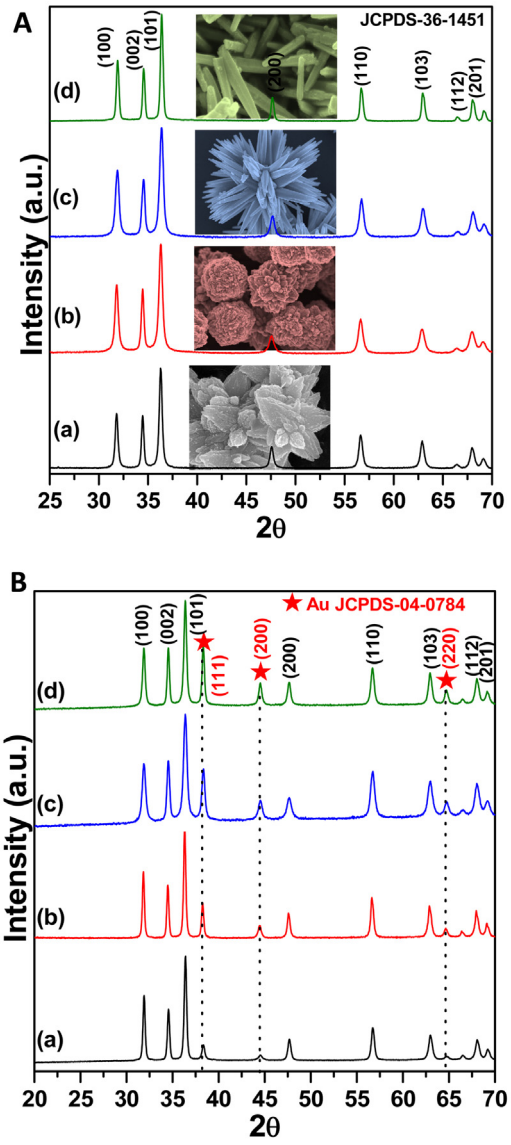


**Fig. 3.** (A) Powder X-ray diffraction patterns of as-prepared ZnO nanostructures (a) nanostars, (b) marigold flower, (c), nanorods assembled flowers and (d) nanorods; (B) Powder X-ray diffraction patterns of ZnO nano-stars/gold composites (a) ZnO/Au 1 wt%, (b) ZnO/Au 2 wt%, (c) ZnO/Au 3 wt%, and (d) ZnO/Au 4 wt%.

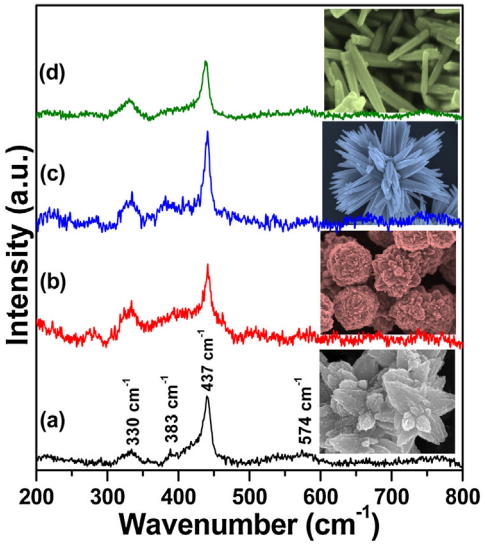


**Fig. 4.** Room temperature micro-Raman spectra of as synthesized ZnO nanostructures (a) nano-stars, (b) marigold flower, (c), nano rods flowers and (d) nano rods.

phonon ($E_2$high- $E_2$low) scattering arising due to the overtones or combination of first order modes [44,45]. The Raman band at 574 $cm^{-1}$ corresponding to $A_1$ (LO) phonon mode is associated with the presence of oxygen vacancies [46,47].

In order to investigate the chemical state and elemental composition of zinc oxide nanostars and zinc oxide nanostars/Au composites, X-ray photo electron spectroscopy analysis (Fig. 5) was carried out in which $C_{1s}$ (284.4 eV) was used for the calibration. The survey spectrum (Inset: Fig. 5a) reveals the existence of photo electron peaks of Zn, O, Au and $C_{1s}$. The remaining smaller peaks are satellite shake-ups of the assigned components [48]. The high resolution core level spectra of Zn 2p region (Fig. 5a) clearly indicates the characteristic symmetric peaks at 1021.38 eV and 1044.47 eV corresponding to (Zn $2p_{3/2}$) and (Zn $2p_{1/2}$) evidently illustrating that the zinc species are in the normal oxidation state of $Zn^{2+}$ in zinc oxide. The core level spectra of oxygen in $O_{1s}$ region (Fig. 5b) reveals the peak, which can be de-convulated and assigned to the lattice oxygen in crystalline zinc oxide (530.2 eV), chemisorbed oxygen caused by the surface hydroxyl groups (531.4 eV) and small binding energy contributions from adsorbed molecular oxygen (532.7) [49]. The core level binding energy of $Zn_{3p}$ and $Au_{4f}$ electrons are shown in Fig. 5c which is de-convoluted into three peaks. The peak centred at 91.9 eV is corresponds to Zn $3p_{1/2}$. The other two peaks located at 83.6 eV and 87.3 eV are attributed to Au $4f_{7/2}$ and $4f_{5/2}$ which is found to be slightly shifted towards the lower binding energy in comparison to 84 eV of the bulk Au. It is generally believed that this small shift is caused by strong electronic interaction (plasmonic effect) between Au and zinc oxide [50–55].

The optical band gap of the as prepared zinc oxide nanostructures were characterised through ultra violet-diffused reflectance spectroscopy (Fig. S2A) in the% of reflectance mode. Zinc oxide is known as an indirect semiconductor; and the band gap energies can be estimated from plot of $(\alpha h\nu)^{1/2}$ versus photon energy ($h\nu$). The relationship between the absorption coefficient ($\alpha$) and incident photon energy ($h\nu$) can be written as $\alpha = A(h\nu - Eg)^2/h\nu$, where $A$ is the absorption constant, ($\alpha$) is the absorption coefficient, h is the planks constant, $\nu$ is the wave number and $E_g$ is the band gap of the material [56,57]. The calculated band gaps (~3.33 eV, 3.33 eV, 3.35, and 3.36 eV for nanostars, marigold flower, nanorods assembled flower, and nanorods respectively) are exactly matches with the reported value of the zinc oxide [58]. The diffuse reflectance spectrum (Fig. S2B)of ZnO nanostars/Au composites exhibits two adsorption regions, the sharp edge ~384 nm due to band edge adsorption of zinc oxide and broad adsorption in the visible region ~560 nm resulting from the characteristics surface plasmon adsorption of Au nanoparticles.

The surface area and pore size distribution of as prepared zinc oxide nanostructures were characterised by $N_2$ adsorption/desorption isotherm method. The adsorption-desorption (Fig. 6) profile exhibits typical type-IV isotherms hysteresis loops, indicating the mesoporous nature of the sample. The inset shows the corresponding pore size distribution ranging from 5 to 50 nm, and the average pore diameter is ~2–10 nm. The calculated surface area of nanostars, marigold flower, nanorods assembled flower and nanorods are 23.67, 19.67, 7.04, 4.52 $m^2/g$ respectively.

## 5. Gas sensing characteristics

It is well established that the sensor response of a semiconducting metal oxide gas sensor is highly affected by the operating temperature where the temperature dependent, adsorption-

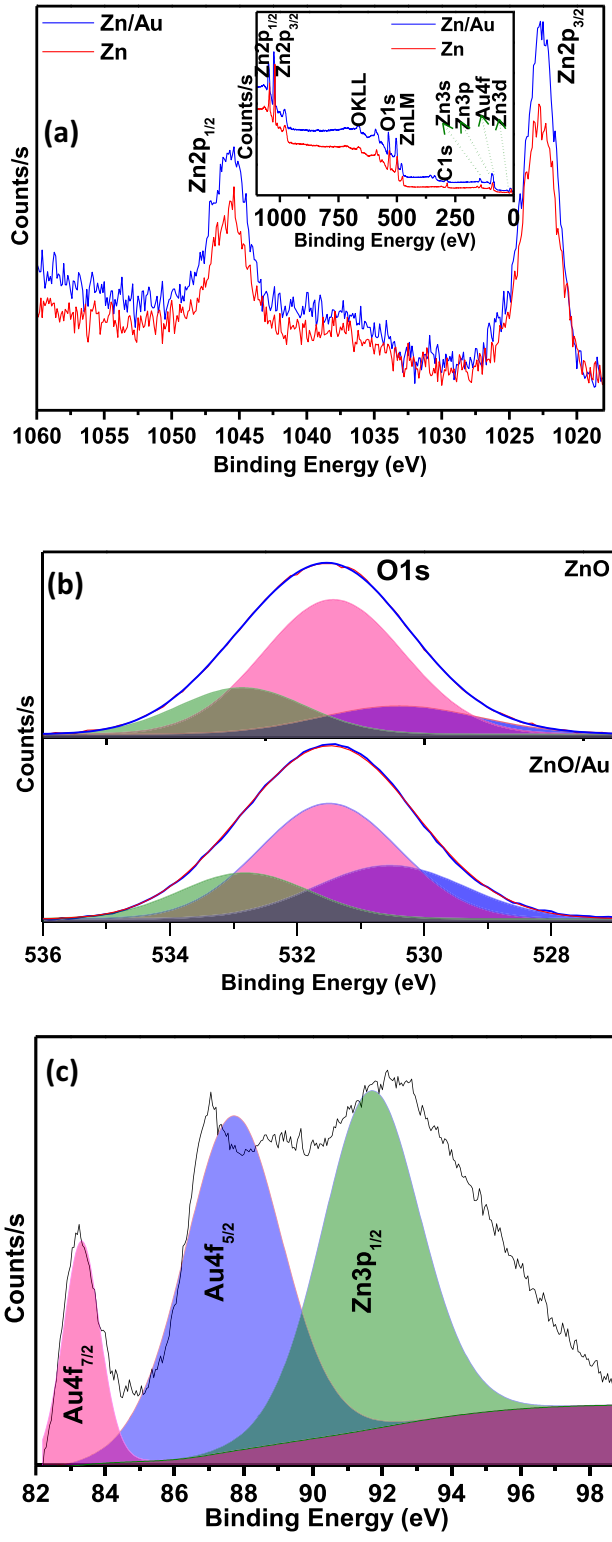


**Fig. 5.** X-Ray photo electron spectroscopy analysis of as prepared zinc oxide nanostars and zinc oxide nanostars/Au composites, (a) core level spectra of zinc (Inset: survey spectra), (b) oxygen core level spectra and (c) core level spectra of zinc and gold in Zn 3p and Au 4f region.

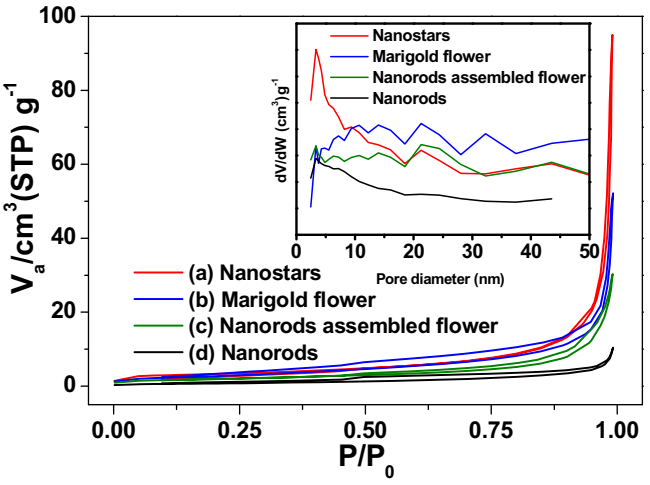


**Fig. 6.** Surface area and pore size distribution of as prepared zinc oxide nanostructures, (a) nanostars, (b) marigold flower, (c), nanorods assembled flowers and (d) nanorods, [Inset: corresponding pore size distributions].

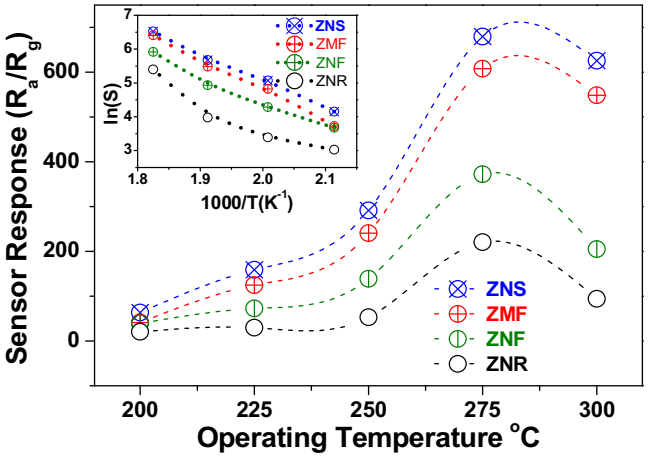


**Fig. 7.** Sensing response characteristics of zinc oxide nanostructures such as nanostars (ZNS), marigold flower (ZMF), nanorods assembled flowers (ZNF), and nanorods (ZNR) as a function of different operating temperatures towards 1000 ppm of CO; [Inset: Arrhenius plot depicting the sensor response].

desorption kinetic process are optimum [59]. Therefore, to find the optimum operating temperature the sensor fabricated by using zinc oxide nanostars, marigold flower, nanorods assembled flower, and nanorods were tested towards 1000 *ppm* of CO as a function of different sensing temperatures (200 °C < Ts >300 °C). Sensor response is defined as $S_R = R_a/R_g$, where $R_a$ is the sensor resistance in air and $R_g$ is the sensor resistance in the presence of gas. The sensor responses of nanostars, marigold flower, nanorods assembled flowers, and nanorods sensors show the typical *n*-type (decrease in resistance) behaviour *i.e.* increasing sensing response with increasing operating temperature. From the sensor response curve (Fig. 7) it is evident that, at each sensing temperature nanostars sensor exhibits a much higher sensor response than the other zinc oxide morphologies. At the elevated sensing temperature ($T_s$ = 275 °C), the nanostars sensor offers a maximum sensitivity of $S_R \sim 681$, whereas the sensor response of marigold flower, nanorods assembled flowers, and nanorods are found to be ~600, ~375, and ~275. The Arrhenius plots of the sensor response, ln(S) vs Ts (sensing temperature), clearly indicates the strong linear dependence in the sensor response as a function of operating temperature (Inset: Fig. 7).

The response and recovery time is considered as one of the primary factor in evaluating the gas sensor performances. Response time ($\Gamma_{RES}$) of the sensor is defined as the time taken by the sensor to reach 90% of its saturation limit after exposure to test gas, while, the recovery time ($\Gamma_{REC}$) is defined as the time necessary for the sensor to reach 10% of its original resistance value once the target

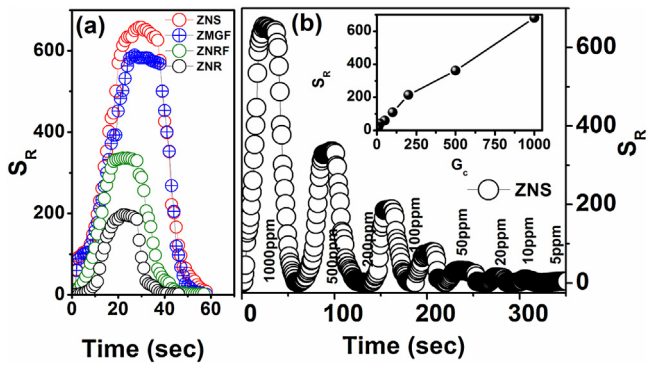


**Fig. 8.** (a) Dynamic sensing response representing the response and recovery time of fabricated zinc oxide sensors such as nanostars, marigold flower, nanorods assembled flower, and nanorods at 275 °C towards 1000 ppm of CO; and (b) Dynamic sensor response of zinc oxide nanostars (ZNS) as function of different gas concentration at operating temperature of 275 °C. [$S_R$: Sensor response, Gc: Gas concentration].

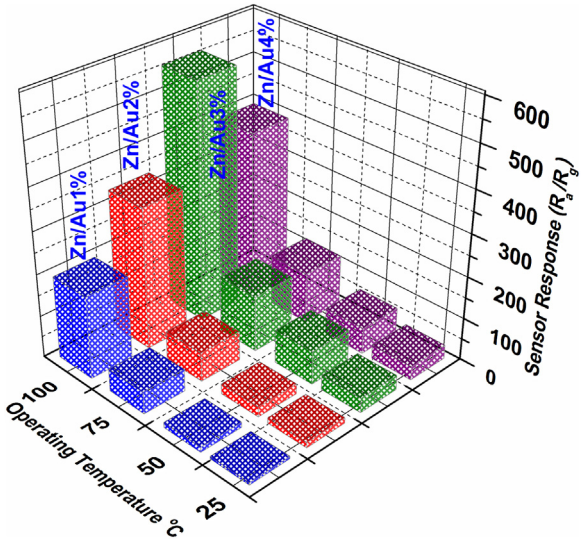


**Fig. 9.** Sensor response of ZnO/Au nanostars toward 500 ppm of CO as a function of different operating temperature.

gas is switched off. The CO response-recovery times ($\Gamma_{RES}$ – $\Gamma_{REC}$) of all four fabricated zinc oxide sensors are presented in Fig. 8(a). The response and recovery time of each sensor toward 1000 *ppm* of CO are estimated to be 21, 23, 17, 16 s and 12, 13, 8, 7 s, respectively. Though the studies unambiguously demonstrate that all the sensing elements possess good capability for the detection of CO, the sensor fabricated using the mesoporous nanostars exhibited much higher response $S_R \sim 681$ with the faster response ($\Gamma_{RES}$) and recovery time ($\Gamma_{REC}$) of 21 s and 12 s. The above investigations directly imply that the magnitude of sensor response is greatly influenced by the morphology of zinc oxide nanostructures, and the sensing performance of nanostars is far superior to the other morphologies. The enhancement in sensitivity of the zinc oxide nanostars is attributed to the high surface area and porosity.

In order to identify the maximum sensitivity of nanostars, further gas sensing analysis were carried out at the elevated temperature ($T_s = 275$ °C) as a function of different gas concentration ($G_C$ ~1000, 500, 200, 100, 50, 20, 10, 5 *ppm* of CO). The dynamic sensor response (Fig. 8(b)) clearly demonstrates the gradual augmentation of sensor response with the increase of the gas concentration. After exposure to air, the sensor responses drop off to the baseline, indicating a good repeatability and reproducibility of the sensors. The nanostars sensor exhibits the highest response of $S_R$ ~681 on exposure to 1000 *ppm*, whereas the lowest response of $S_R$ ~15 were observed toward 5 *ppm* of CO indicating the wider range of detection limit and its excellent sensing behaviour.

In order to improve the sensing characteristics such as sensitivity, selectivity and to reduce the sensing temperature, different weight percentage of gold nanoparticles were incorporated into the zinc oxide nanostars matrices. Fig. 9 shows the sensor response for the 1, 2, 3, and 4 wt% Au loaded zinc oxide nanostars as a function of operating temperature towards 500 *ppm* of CO. As evident from Fig. 9 the sensor response increases with increasing gold concentration from 1 to 3 wt%. A loading of 1 wt% of Au nanoparticles was enough to bring down the operating temperature and the maximum sensor response observed at room temperature ($T_S = 35$ °C) is $S_R \sim 5.3$. The sensor response of 3 wt% Au loaded zinc oxide nanostars is up to $S_R \sim 35$ at 35 °C and $S_R \sim 562$ at 100 °C respectively. However, further loading of gold content is leading to lowering down the sensor response. This can be explained based on the following lines. Uniformly distributed Au nanoparticles on zinc oxide nanostars matrices have a remarkable influence on the sensor performances. Incorporating the higher amount of Au nanopartilces on zinc oxide nanostars may affect the active surface area of zinc oxide due to the masking and agglomeration of Au nanoparticles [54]. Therefore, the optimized 3 wt% Au nanoparticles loaded zinc oxide nanostars were selected for further analysis.

Fig. 10 shows the dynamic sensor response of 3 wt% Au incorporated zinc oxide nanostars sensor as a function of different gas concentration at 35 °C and 75 °C respectively. As expected the sensor response gradually increases with increasing the gas concentration and completely recovered to the initial value after the removal of CO gas. ZnO nanostars/Au 3 wt% sensor shows the broad range detection limit at RT (Fig. 10a). The sensor responses to CO gas were quite stable and reproducible for the repeated test cycles. The ZnO nanostars/Au 3 wt% sensor showed responses of ~8.16, 14.87, 24.52, and 55.03 toward 50, 100, 200, and 500 *ppm* of CO at 35 °C. In contrast, the sensor responses are found to be increased to ~33.21, 64.53, 93.09, and 208 toward 50, 100, 200, and 500 *ppm* of CO at 75 °C (Fig. 10b). The CO response-recovery times ($\Gamma_{RES}$ – $\Gamma_{REC}$) of the sensor (Fig. 10(c, d)) at 75 °C for 500 *ppm* of CO is about ~54 and ~37 s, whereas the sensor response ($\Gamma_{RES}$) at 35 °C is ~41 s and the corresponding recovery time ($\Gamma_{REC}$) is 40 s. Selectivity of the ZnO nanostars/Au 3 wt% was tested in the presence of other reducing gases, including methanol, ethanol, acetone, hydrogen with a gas concentration of 50 *ppm* at 35 °C. As seen in Fig. S3, the sensor responds significantly very low to the other interfering gases compare to CO. The sensor response to CO ($S_R \sim 8.1$) is almost 4, 5, 5 and 7 times higher than to methanol, ethanol, acetone and $H_2$ indicating the strong selectivity of the sensor toward CO at RT. To investigate the effect of humidity on the sensor response further gas sensing analysis were carried out ~35 °C towards 500 ppm of CO at different%RH (Fig. S4). The sensor response at dry air environment is S~35 and it found to be S ~ 32, 29, and 25 at 30, 50 and 70% of RH. For practical applications, the gas-sensing stability needs to be verified to ensure the long-term reliability of the sensor. To evaluate the long-term stability the sensor were tested daily towards 100 ppm of gas at 35 °C for 50 days. The sensing measurement analysis (Fig. S5) shows repeatable sensor response with only a small fluctuation indicating the excellent repeatability of the fabricated Au/ZnO sensor.

## 6. Generalised sensing mechanism

The enhanced sensing response of zinc oxide nanostars and Au loaded zinc oxide nanostars sensor could be explained based on the following lines. As discussed in the preceding section, the nanostars

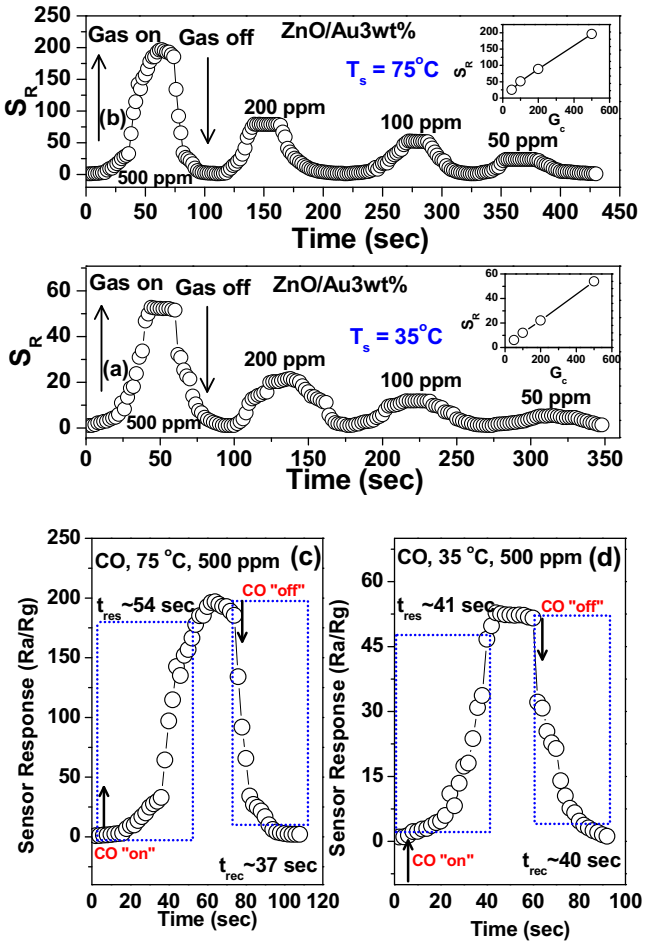


**Fig. 10.** Dynamic sensor response of ZnO nanostars/Au 3 wt% as a function of different gas concentrations at (a) 35 °C and (b) 75 °C; (c, d) Dynamic sensor response characteristics depicting the response and recovery time of ZnO/Au 3 wt% sensor toward 500 ppm of CO at different operating temperature (c) 75 °C and (d) 35 °C. [$G_C$-Gas Concentration; $S_R$-Sensor Response; $T_S$-Sensing Temperature].

are composed of numerous ultrafine nanoparticles of size ~20 nm which provides more active sites for adsorption of molecular oxygen. When the operating temperature of the sensor element was increased, the adsorbed oxygen gets ionized by extracting electrons from the conduction band of zinc oxide and creating chemisorbed reactive oxygen species ($O_2^-$, $O^-$, $O^{2-}$) which leads to the increase in electrical resistance of the sensing material. Upon the sensor exposed to CO, it gets oxidized by reactive oxygen species from the surface of the material and release electrons into the conduction band of zinc oxide. Due to this process n-type zinc oxide will be more negative, thus leads to narrowing of depletion layer which results in the decrease in electrical resistance of the zinc oxide. Further, the sensor response is greatly improved by the incorporation of gold nanoparticles. The enhanced sensing response at room temperature could be attributed by the following two rationales: (i) spillover effect and (ii) work function modulations. The electron rich sites of gold nanoparticles on the surface of zinc oxide nanostars catalytically interact with oxygen by transferring electrons from the conduction band to the adsorbed oxygen atoms, forming reactive oxygen species ($O_2^-$, $O_2^-$, and $O^-$). This is then spilled onto metal oxide surface even at room temperature. This elucidate why the optimum sensing temperature decreases with increasing amount of gold nanopartilces [60,61]. This chemical sensitization is the predominant mechanism for the gold decorated zinc oxide to detect CO. Another important function of Au nanopartilces is the work function modulations. After decorating gold nanoparticles on the surface of zinc oxide strong electronic interaction was formed between gold and the defect sites of zinc oxide. This creates the nanoscopic depletion region at metal and metal oxide interface, which alter the Schottky barrier height [62,63]. This localized depletion regions around metal and metal oxide interface enhancing the sensor response for the gas detection. In the oxygen environment, adsorbed oxygen traps the electron from the conduction band ($O_2^-$, $O_2^-$, and $O^-$) and significantly magnifies the Schottky barrier height and thus the electrical resistance of the sensor is increases. Upon the CO exposure ($O^- + CO - CO_2 + e^-$) the Schottky barrier height is decreases and a lower the sensor resistance. This dramatically changed Schottky barrier height also contributes to the enhanced CO gas sensing. Fig. 11 shows the representative energy band diagram of the zinc oxide nanostar and Au

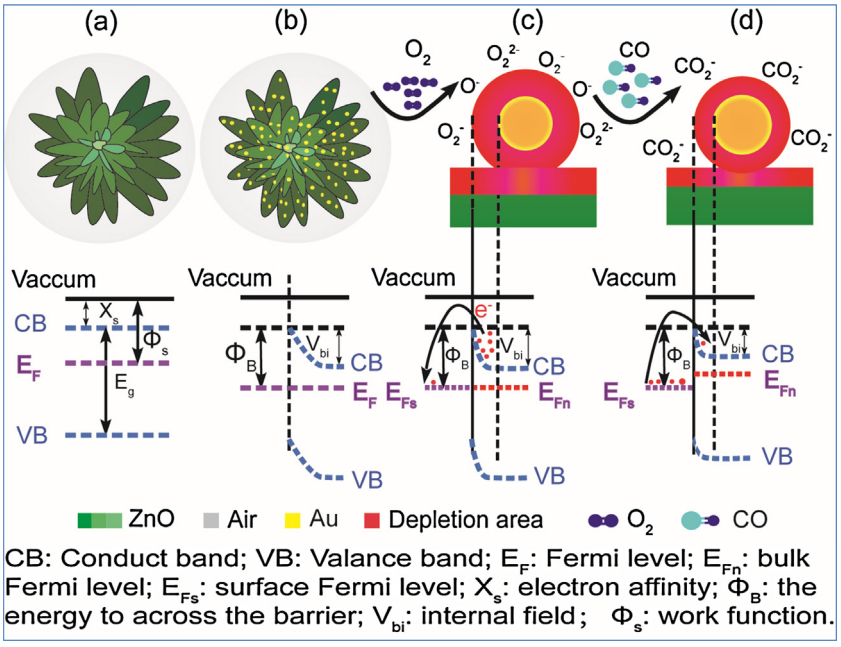


**Fig. 11.** Energy band diagram of zinc oxide nanostar and Au nanopartilces incorporated zinc oxide nanostar before and after CO exposure.

nanopartilces incorporated zinc oxide nanostar before and after CO exposure is shown as schematic 1. All these factors coupled with the hierarchical architecture with porous structure of the as synthesised zinc oxide provides numerous channels for gas transport and the higher surface to volume ratio giving large accessible surface area for the surface adsorbed chemical kinetics reactions leading the enhanced CO sensing response.

## 7. Proposed sensing mechanism based on FTIR analysis

In order to effectively understand the CO oxidation at room temperature and to found the exact reason behind the enhanced gas sensing response the FTIR analysis was carried out on zinc oxide/Au (ZnO/Au–3 wt%) sensing material before and after exposure to CO gas. This involves the taking the IR spectra of the sample before passing the gas, then the material were exposed to CO (500 ppm at 35 °C) and immediately IR spectra were recorded. Finally ~5–10 min were waited for desorption of CO from the material surface and again recorded for the FTIR spectra.

The FTIR spectra of the as prepared zinc oxide nanostar and zinc oxide/Au3 wt% sensing material before and after passing the CO gas are shown as Fig. S6. Prior to sensing experiments, the FTIR spectra of zinc oxide/Au3 wt% were recorded (Fig. S6(a)) as the reference, then the sensing materials exposed to CO towards 500 ppm of CO at 35 °C and recorded the FTIR spectra (Fig. S6(b)). As seen from the spectrum several bands were observed due to the adsorption-desorption-dissociation of CO on the zinc oxide/Au surface. The band observed at 2014 $cm^{-1}$ is corresponds to the CO-adsorbed on the Au-nanopartilces. The peak at 1548 $cm^{-1}$ can be assigned to the CO species σ-bonded to Au nanoparticles and π-bonded to Zn ions (marked as region-1). The band at 2133 $cm^{-1}$ can be indexed to the CO-adsorbed on the Au oxidized sites. The several bands observed at 1700–1000 $cm^{-1}$ range could assign to carbonate like species (marked as region-2). The band at 2400–2250 $cm^{-1}$ range adsorption bands are observed due to the asymmetric stretching of the different isotopic molecular $CO_2$ formed during the gas sensing [64] (marked as region-3).

This observation is an indication that the two independent pathways are possible for CO oxidation through ZnO/Au composites; (i) due to the catalytic effect of Au, in this process the adsorption-desorption chemical kinetics of CO takes place on the surface of Au nanoparticles and reacts with the readily available molecular oxygen species and converted into the molecular $CO_2$; (ii) the dissociated CO converted into the molecular carbonyl species (Fig. S6(b)) interacts with the Au and Zn through the σ-bond and the π-orbital [65,66]. This process changes the charge state of CO that would easily react with adsorbed molecular oxygen species and get oxidized by generating the delocalised electrons through the following reactions.

$$2CO + {O_2}^-_{ads} \rightarrow 2CO_2 + e^-$$

$$CO + {O^-}_{ads} \rightarrow CO_2 + e^-$$

These delocalised electrons are back-transfer to the conduction band of ZnO which leads to the higher sensing performance [67,68]. Finally the sensing material were allowed for desorption of CO from the sensing material for 5–10 min and then the FTIR spectra were recorded. As observed from the FTIR analysis the CO, $CO_2$ and the other intermediate ${CO_3}^{2-}_{ads}$ Peaks are getting disappeared after 5 and 10 min desorption of CO (Fig. S6(c, d)) indicating the complete recovery of the ZnO/Au sensing material. Where as the pure zinc oxide sensing material shows no significant difference in the spectra before and after passing the gas (Fig. S6(e, f)) indicating that the there is no significant CO oxidation at room temperature.

## 8. Conclusion

In summary, we have successfully demonstrated a facile hydrothermal synthetic strategy to obtain the exotic super structural hierarchical zinc oxide with impressive unique architectures. Appreciable control on the morphology and self-assembly of nanostructures was achieved by the controlled variation of the $Zn^{2+}$/ethanolamine mole ratio. The as prepared materials were characterised in detail by several analytical techniques and the findings from XRD, micro-Raman, XPS, and UV-DRS analysis were consistent with each other. The as prepared zinc oxide architectures were investigated in detail their gas sensing characteristics towards CO by evaluating the sensitivity, sensor response, and recovery time. At an optimum sensing temperature ($T_S$ = 275 °C) zinc oxide nanostars exhibits maximum sensor response of $S_R$~ 681. The sensor response of marigold flower, nanorods assembled flower, and nanorods are ~600, ~375, and ~275 respectively. The zinc oxide nanostars sensors exhibits the wide range of detection limit ($S_R$ ~ 681 to 1000 *ppm* and $S_R$ ~ 31 to 5 *ppm* of CO) indicating its excellent sensing behaviour. Zinc oxide nanostar sensor able to sense CO at room temperature ($T_S$ ~ 35 °C) by incorporating only 3 wt% of gold nanoparticles and it exhibits enhanced sensing response ($S_R$ ~15 toward 50 *ppm*) at 35 °C with an excellent response ($\Gamma_{RES}$ ~8 s) and recovery ($\Gamma_{REC}$ ~15 s) time. The sensor also shows excellent selectivity ($S_R$ ~ 8.1 to 50 *ppm* of CO) is almost 4, 5, 5 and 7 times higher than to other interfering gases such as methanol, ethanol, acetone and $H_2$ indicating the strong selectivity of the sensor toward CO.

## Acknowledgements

This work was supported by the National Research Foundation of Korea (NRF) grant funded by the Korea government (No.2015R1A4A1041746). Authors are also thankful to Prof. Sun-Ju Song and Mr. In-Ho Kim, School of Materials Science and Engineering, Chonnam National University for their help and support in FTIR analysis.

## Appendix A. Supplementary data

Supplementary data associated with this article can be found, in the online version, at http://dx.doi.org/10.1016/j.snb.2016.11.152.

## References

[1] D.D. Lee, D.S. Lee, Environmental gas sensors, IEEE Sens. J. 1 (2001) 214–224.
[2] Y. Liu, J. Parisi, X. Sun, Y. Lei, Solid state gas sensors for high temperature applications –a review, J. Mater. Chem. A 2 (2014) 9919–9943.
[3] G. Zhang, L. Dang, L. Li, R. Wang, H. Fu, K. Shi, Design and construction of $Co_3O_4$/PEI–CNTs composite exhibiting fast responding CO sensor at room temperature, CrystEngComm 15 (2013) 4730–4738.
[4] T. Zhang, L. Liu, Q. Qi, S. Li, G. Lu, Development of microstructure In/Pd-doped $SnO_2$ sensor for low-level CO detection, Sens. Actuators. B 139 (2009) 287–291.
[5] J.H. Zhang, X.H. Liu, G. Neri, N. Pinna, Nanostructured materials for room-temperature gas sensors, Adv. Mater. 28 (2016) 795–831.
[6] S. Thirumalairajan, K. Girija, V.R. Mastelaro, N. Ponpandian, Surface morphology-dependent room-temperature $LaFeO_3$ nanostructure thin films as selective $NO_2$ gas sensor prepared by radio frequency magnetron sputtering, ACS Appl. Mater. Interfaces 6 (2014) 13917–13927.
[7] A. Shanmugasundaram, P. Basak, L. Satyanarayana, S.V. Manorama, Hierarchical SnO/$SnO_2$ nanocomposites: formation of in situ p–n junctions and enhanced $H_2$ sensing, Sens. Actuators B 185 (2013) 265–273.
[8] H. Kawasaki, T. Ueda, Y. Suda, T. Ohshima, Properties of metal doped tungsten oxide thin films for NOx gas sensors grown by PLD method combined with sputtering process, Sens. Actuators B 100 (2004) 266–269.
[9] N.V. Hieua, L.T.B. Thuy, N.D. Chien, Highly sensitive thin film $NH_3$ gas sensor operating at room temperature based on $SnO_2$/MWCNTs composite, Sens. Actuators B 129 (2008) 888–895.
[10] Q. Lin, Y. Li, M. Yang, Tin oxide/graphene composite fabricated via a hydrothermal method for gas sensors working at room temperature, Sens. Actuators B 173 (2012) 139–147.

[11] X. Liu, J. Zhang, X. Guo, S. Wu, S. Wang, Amino acid-assisted one-pot assembly of Au, Pt nanoparticles onto one-dimensional ZnO microrods, Nanoscale 2 (2010) 1178–1184.
[12] N. Gogurla, A.K. Sinha, S. Santra, S. Manna, S.K. Ray, Multifunctional Au-ZnOplasmonic nanostructures for enhanced UV photodetector and room temperature NO sensing devices, Sci. Rep. 4 (2014) 6483, http://dx.doi.org/10.1038/srep06483.
[13] S. Santra, et al., ZnO nanowires grown on SOI CMOS substrate for ethanol sensing, Sens. Actuators B 146 (2010) 559–565.
[14] X. Zou, J. Wang, X. Liu, C. Wang, Y. Jiang, Y. Wang, X. Xiao, J.C. Ho, J. Li, C. Jiang, Y. Fang, W. Liu, L. Liao, Rational design of sub-parts per million specific gas sensors array based on metal nanoparticles decorated nanowire enhancement mode transistor, Nano Lett. 13 (2013) 3287–3292.
[15] X.H. Liu, J. Zhang, X. Guo, S.H. Wang, S. Wu, Core–shell a–$Fe_2O_3$@$SnO_2$/Au hybrid structures and their enhanced gas sensing properties, RSC Adv. 2 (2012) 1650–1655.
[16] J. Shin, S.J. Choi, I. Lee, D.Y. Youn, C.O. Park, J.H. Lee, H.L. Tuller, I.D. Kim, Thin-wall assembled $SnO_2$ fibers functionalized by catalytic Pt nanoparticles and their superior exhaled-breath-sensing properties for the diagnosis of diabetes, Adv. Funct. Mater. 23 (2013) 2357–2367.
[17] Y. Yu, J. Zhang, X. Wu, W. Zhao, B. Zhang, Nanoporous single-crystal-like cd(x)zn(1-x)s nanosheets fabricated by the cation-exchange reaction of inorganic-organic hybrid zns-amine with cadmium ions, Angew. Chem. Int. Ed. 51 (2012) 897–900.
[18] X.H. Liu, J. Zhang, T. Yang, L. Wang, Y. Kang, S. Wang, S.H. Wu, Self-assembled hierarchical flowerlike ZnO architectures and their gas-sensing properties, Powder Technol. 217 (2012) 238–244.
[19] R. Zou, G. He, K. Xu, Q. Liu, Z. Zhang, J. Hu, ZnO nanorods on reduced graphene sheets with excellent field emission, gas sensor and photocatalytic properties, J. Mater. Chem. A 1 (2013) 8445–8452.
[20] R. Kumar, O. Al-Dossary, G. Kumar, A. Umar, Zinc oxide nanostructures for $NO_2$ gas sensor applications: a review, Nano Micro Lett. 7 (2015) 97–120.
[21] R.F. Service, Will UV lasers beat the blue, Science 276 (1997) 895.
[22] S.J. Pearton, D.P. Norton, K. Ip, Y.W. Heo, T. Steiner, Recent progress in processing and properties of ZnO, Prog. Mater. Sci. 50 (2005) 293–340.
[23] Y.J. Chen, X.Y. Xue, Y.G. Wang, T.H. Wang, Synthesis and ethanol sensing characteristics of single crystalline $SnO_2$ nanorods, Appl. Phys. Lett. 87 (2005) (233503- 233503-3).
[24] C.C. Li, Z.F. Du, L.M. Li, H.C. Yu, Q. Wan, T.H. Wang, Surface-depletion controlled gas sensing of ZnO nanorods grown at room temperature, Appl. Phys. Lett. 91 (2007) (032101- 032101-3).
[25] X. Wang, F. Sun, Y. Duan, Z. Yin, W. Luo, Y. Huang, J. Chen, Highly sensitive, temperature-dependent gas sensor based on hierarchical ZnO nanorod arrays, J. Mater. Chem. C 3 (2015) 11397–11405.
[26] Z. Zhang, X. Li, C. Wang, L. Wei, Y. Liu, C. Shao, ZnO hollow nanofibers: fabrication from facile single capillary electro spinning and applications in gas sensors, J. Phys. Chem. C 113 (2009) 19397–19403.
[27] S. Tian, F. Yang, D. Zeng, C. Xie, Solution-processed gas sensors based on ZnO nanorods array with an exposed (0001) facet for enhanced gas-sensing properties, J. Phys. Chem. C 116 (2012) 10586–10591.
[28] M. Yin, S. Liu, Preparation of ZnO hollow spheres with different surface roughness and their enhanced gas sensing property, Sens. Actuators B 197 (2014) 58–65.
[29] A.R. Phani, S.V. Manorama, V.J. Rao, X-ray photoelectron spectroscopy studies on Pd doped $SnO_2$ liquid petroleum gas sensor, Appl. Phys. Lett. 71 (1997) 2358–2360.
[30] X.H. Liu, J. Zhang, X.Z. Guo, S.H. Wu, S.R. Wang, Amino acid-assisted one-pot assembly of Au, Pt nanoparticles onto one-dimensional ZnO microrods, Nanoscale 2 (2010) 1178–1184.
[31] J. Zhang, X.H. Liu, X.Z. Guo, S.H. Wu, S.R. Wang, A general approach to fabricate diverse noble-metal (Au, Pt Ag, Pt/Au)/$Fe_2O_3$ hybrid nanomaterials, Chem. Eur. J. 16 (2010) 8108–8116.
[32] A. Kolmakov, D.O. Klenov, Y. Lilach, S. Stemmer, M. Moskovits, Enhanced gas sensing by individual $SnO_2$ nanowires and nanobelts functionalized with Pd Catalyst Particles, Nano Lett. 5 (2005) 667–673.
[33] R.L. Vander Wal, G.W. Hunter, J.C. Xu, M.J. Kulis, G.M. Berger, T.M. Ticich, Metal-oxide nanostructure and gas-sensing performance, Sens. Actuators B 138 (2009) 113–119.
[34] R.K. Joshi, Q. Hu, F. Alvi, N. Joshi, A. Kumar, Au decorated zinc oxide nanowires for CO sensing, J. Phys. Chem. C 113 (2009) 16199–16202.
[35] X. Wang, Q. Zhang, Q. Wan, G. Dai, C. Zhou, B. Zou, Controllable ZnO architectures by ethanolamine-assisted hydrothermal reaction for enhanced photocatalytic activity, J. Phys. Chem. C 115 (2011) 2769–2775.
[36] C. Balamurugan, S. Arunkumar, D.-W. Lee, Hierarchical 3D nanostructure of $GdInO_3$ and reduced-graphene-decorated $GdInO_3$nanocomposites for CO sensing applications, Sens. Actuators B 234 (2016) 155–166.
[37] L. Shi, J.T.N. Anupriya, B.M.G. Josephine, C. Tighe, R. Gruar, R. Binions, I. Parkin, J. Darr, Highly sensitive ZnO nanorod- and nanoprism-based $NO_2$ gas sensors: size and shape control using a continuous hydrothermal pilot plan, Langmuir 29 (2013) 10603–10609.
[38] X. Li, C. Wang, H. Guo, P. Sun, F. Liu, X. Liang, G. Lu, Double-shell architectures of $ZnFe_2O_4$ nanosheets on ZnO hollow spheres for high-performance gas sensors, ACS Appl. Mater. Interfaces 7 (2015) 17811–17818.
[39] S.M. Majhi, P. Rai, Y.-T. Yu, Facile approach to synthesize Au@ZnO core-shell nanoparticles and their application for highly sensitive and selective gas sensors, ACS Appl. Mater. Interfaces 7 (2015) 9462–9468.
[40] X. Li, X. Zhou, H. Guo, C. Wang, J. Liu, P. Sun, F. Liu, G. Lu, Design of Au@ZnO yolk-shell nanospheres with enhanced gas sensing properties, ACS Appl. Mater. Interfaces 6 (2014) 18661–18667.
[41] S.-S. Lo, D. Huang, Morphological variation and Raman spectroscopy of ZnO hollow microspheres prepared by a chemical colloidal process, Langmuir 26 (2010) 6762–6766.
[42] Z. Dai, K. Liu, Y. Tang, X. Yang, J. Bao, J. Shen, A novel tetragonal pyramid-shaped porous ZnO nanostructure and its application in the biosensing of horseradish peroxidise, J. Mater. Chem. 18 (2008) 1919–1926.
[43] G.M. Kumar, P. Ilanchezhiyan, J. Kawakita, M. Subramanian, R. Jayavel, Magnetic and optical property studies on controlled low-temperature fabricated one-dimensional Cr doped ZnO nanorods, CrystEngComm 12 (2010) 1887–1892.
[44] R. Cusco, E.A. Llado, J. Ibanez, L. Artus, J. Jimenez, B. Wang, M.J. Callahan, Temperature dependence of Raman scattering in ZnO, Phys. Rev. B 75 (2007) (165202-165202-11).
[45] S. Bai, J. Hu, D. Li, R. Luo, A. Chen, C.C. Liu, Quantum-sized ZnO nanoparticles: synthesis, characterization and sensing properties for $NO_2$, J. Mater. Chem. 21 (2011) 12288–12294.
[46] G.J. Exarhos, S.K. Sharma, Influence of processing variables on the structure and properties of ZnO films, Thin Solid Films 270 (1995) 27–32.
[47] B. Li, H. Cao, ZnO@graphene composite with enhanced performance for the removal of dye from water, J. Mater. Chem. 21 (2011) 3346–3349.
[48] T. Wang, B. Jin, Z. Jiao, G. Lu, J. Yeb, Y. Bi, Photo-directed growth of Au nanowires on ZnO arrays for enhancing photoelectrochemical performances, J. Mater. Chem. A 2 (2014) 15553–15559.
[49] T.H. Yang, L.D. Huang, Y.W. Harn, C.C. Lin, J.K. Chang, C.I. Wu, J.M. Wu, High density un aggregated Au nanoparticles on ZnO nanorod arrays function as efficient and recyclable photocatalysts for environmental purification, Small 9 (2013) 3169–3182.
[50] M. Ahmad, S. Yingying, A. Nisar, H. Sun, W. Shen, M. Wei, J. Zhu, Synthesis of hierarchical flower-like ZnO nanostructures and their functionalization by Au nanoparticles for improved photocatalytic and high performance Li-ion battery anodes, J. Mater. Chem. 21 (2011) 7723–7729.
[51] X.-J. Wang, W. Wang, Y.-L. Liu, Enhanced acetone sensing performance of Au nanoparticles functionalized flower-like ZnO, Sens. Actuators B 168 (2012) 39–45.
[52] J. Zhang, X. Liu, S. Wu, B. Cao, S. Zheng, One-pot synthesis of Au-supported ZnO nanoplates with enhanced gas sensor performance, Sens. Actuators B 169 (2012) 61–66.
[53] S. Kuriakose, B. Satpatib, S. Mohapatra, Enhanced photocatalytic activity of Co doped ZnO nanodisks and nanorods prepared by a facile wet chemical method, Phys. Chem. Chem. Phys. 16 (2014), 12741–1274.
[54] G.M. Kumar, P. Ilanchezhiyan, J. Kawakita, M. Subramanian, R. Jayavel, Magnetic and optical property studies on controlled low-temperature fabricated one-dimensional Cr doped ZnO nanorods, CrystEngComm 12 (2010) 1887–1892.
[55] C. Yu, Q. Hao, S. Saha, L. Shi, X.Y. Kong, Z.L. Wang, Integration of metal oxide nanobelts with microsystems for nerve agent detection, Appl. Phys. Lett. 86 (2005) (063101-1-063101-3).
[56] F. Demichelis, E.M. Mezzetti, V. Smurro, A. Tagliaferro, E. Tresso, Physical properties of chemically sprayed tin oxide and indium tin oxide trans-parent conductive films, J. Phys. D: Appl. Phys. 18 (1985) 1825–1832.
[57] A.E. Morales, E.S. Mora, U. Pal, Use of diffuse reflectance spectroscopy for optical characterization of un-supported nanostructures, Revista Mexicana De Fisica S. 53 (2007) 18–22.
[58] Y.C. Chang, H.-W. Wu, H.-L. Chen, W.-Y. Wang, L.-J. Chen, Two-dimensional inverse opal ZnO nanorod networks with photonic band gap, J. Phys. Chem. C 113 (2009) 14778–14782.
[59] Q. Xiang, G.F. Meng, H.B. Zhao, Y. Zhang, H. Li, W.J. Ma, J.Q. Xu, Au nanoparticle modified $WO_3$ nanorods with their enhanced properties for photocatalysis and gas Sensing, J. Phys. Chem. C 114 (2010) 2049–2055.
[60] J.C. Belmonte, J. Manzano, J. Arbiol, A. Cirera, J. Puigcorbe, A. Vila, N. Sabate, I. Gracia, C. Cane, J.R. Morante, Micromachined twin gas sensor for CO and $O_2$ quantification based on catalytically modified nano-$SnO_2$, Sens. Actuators B 114 (2006) 881–892.
[61] A. Dieguez, A. Vila, A. Cabot, A.R. Rodriguez, J.R. Morante, J. Kappler, N. Barsan, U. Weimar, W. Goepel, Influence on the gas sensor performances of the metal chemical states introduced by impregnation of calcinated $SnO_2$ sol?gel nanocrystals, Sens. Actuators B 68 (2000) 94–99.
[62] N. Singh, R.K. Gupta, P.S. Lee, Gold-nanoparticle-functionalized $In_2O_3$ nanowires as CO gas sensors with a significant enhancement in response, ACS Appl. Mater. Interfaces 3 (2011) 2246–2252.
[63] V.P. Zhdanov, nm-sized metal particles on a semiconductor surface Schottky model, etc, Surf. Sci. Lett. 512 (2002) 331–334.
[64] F. Boccuzzi, A. Chiorino, S. Tusbota, M. Haruta, An IR study of CO-sensing mechanism on Au/ZnO, Sens. Actuators B 24–25 (1995) 540–543.
[65] A. Chiorino, G. Ghiotti, F. Boccuzzi, Reactivity and electronic properties of two microcrystalline ZnO surfaces: interaction with CO and CO/O2, Vacuum 41 (1990) 16–18.
[66] Pt/ZnO system: I.R. study of the vibrational and electronical effects induced by heating in co atmosphere, Surface sci. 233 1990 141–152.
[67] X. Liu, J. Zhang, L. Wang, T. Yang, X. Guo, S. Wu, S. Wang, 3D hierarchically porous ZnO structures and their functionalization by Au nanoparticles for gas sensors, J. Mater. Chem. 21 (2011) 349–356.

[68] M.C. Kung, R.J. Davis, H.H. Kung, Understanding Au-catalyzed low-temperature CO oxidation, J. Phys. Chem. C 111 (2007) 11767–11775.
[69] M. Hjiri, L. El Mir, S.G. Leonardi, A. Pistone, L. Mavilia, G. Neri, Al-doped ZnO for highly sensitive CO gas sensors, Sens. Actuators B 196 (2014) 413–420.
[70] C. Li, M. Lv, J. Zuo, X. Huang, $SnO_2$ highly sensitive CO gas sensor based on quasi-molecular-imprinting mechanism design, Sensors 15 (2015) 3789–3800.
[71] S.M.A. Durrani, M.F. Al-Kuhaili, I.A. Bakhtiari, M.B. Haider, Investigation of the Carbon Monoxide Gas Sensing Characteristics of tin oxide mixed cerium oxide thin films, Sensors 12 (2012) 2598–2609.
[72] J. Yang, K. Hidajat, S. Kawi, Synthesis, characterization and sensing properties of nano-$SnO_2$ supported on SBA-15 as highly sensitive semiconductor gas sensors, J. Mater. Chem. 19 (2009) 292–298.
[73] S. Pati, A. Maity, P. Banerji, S.B. Majumder, Qualitative and quantitative differentiation of gases using ZnO thin film gas sensors and pattern recognition analysis, Analyst 139 (2014) 1796–1800.
[74] H. Gong, J.Q. Hu, J.H. Wang, C.H. Ong, F.R. Zhu, Nano-crystalline Cu-doped ZnO thin film gas sensor for CO, Sens. Actuators B 115 (2006) 247–251.
[75] Y.S. Kim, I.S. Hwang, S.J. Kim, C.Y. Lee, J.H. Lee, CuO nanowire gas sensors for air quality control in automotive cabin, Sens. Actuators B 135 (2008) 298–303.
[76] H.Y. Lai, C.H. Chen, Highly sensitive room-temperature CO gas sensors: pt and Pd nanoparticle-decorated $In_2O_3$ flower-like nanobundles, J. Mater. Chem. 22 (2012) 13204–13208.
[77] Y.-J. Chiang, F.-M. Pan, PdO nanoflake thin films for CO gas sensing at low temperatures, J. Phys. Chem. C 117 (2013) 15593–15601.
[78] N. Singh, R.K. Gupta, P.S. Lee, Gold-nanoparticle-functionalized $In_2O_3$ nanowires as CO gas sensors with a significant enhancement in response, ACS Appl. Mater. Interfaces 3 (2011) 2246–2252.
[79] L. Dang, G. Zhang, K. Kan, Y. Lin, F. Bai, L. jing, P. Shen, L. Li, K. Shi, Heterostructured $Co_3O_4$/PEI–CNTs composite: fabrication, characterization and CO gas sensors at room temperature, J. Mater. Chem. A 2 (2014) 4558–4565.
[80] N. Du, H. Zhang, X. Ma, D. Yang, Homogeneous coating of Au and $SnO_2$ nanocrystals on carbon nanotubes via layer-by-layer assembly: a new ternary hybrid for a room-temperature CO gas sensor, Chem. Commun. 618 (2008) 6182–6184.

## Biographies

**Dr. S. Arunkumar** did his Ph.D in Physics (specialization in materials science) from CSIR-Indian Institute of Chemical Technology, Hyderabad, India. Currently he is working as a post doctoral researcher at MEMS and Nanotechnology laboratory, School of Mechanical Engineering, Chonnam National University, Gwangju, Republic of Korea. His research interests include design and development of functional nanostructured materials for applications in chemical sensors, catalysis and energy storage devices.

**Tianfeng Hou** did her Masters degree in Material Science and Technology from the Chongqing University of Technology, Chongqing, China in 2015. Currently she is pursuing her doctoral studies at MEMS and Nanotechnology laboratory, School of Mechanical Engineering, Chonnam National University, Republic of Korea. Her research interests mainly focused on tailoring the nanostructured materials for water splitting and gas sensor applications.

**Su Han Park** received his Ph.D. degrees in Mechanical engineering from Hanyang University, Seoul, Korea in 2011. He joined the School of Mechanical engineering at Chonnam National University, Korea in 2014.

**Senghun Jung** joined the School of Mechanical engineering at Chonnam National University, Korea in March 2015. Before joining Chonnam National University, he worked at Battery R&D in LG Chem from 2010 to 2015. He led his Advanced Battery Simulation group and conducted various projects about battery and electric vehicles. He received his doctorate in Mechanical engineering from Pennsylvania State University, and his BA and MS from Seoul National University. Prior to joining academia, he also worked as an industrial consultant in production planning and supply chain management from 2001 to 2003.

**Prof. Dong-Weon Lee** received his Ph.D. degrees in Mechatronics engineering from Tohoku University, Sendai, Japan in 2001. He has been a Professor of Mechanical Engineering at Chonnam National University (CNU), Republic of Korea since 2004. Previously, he was with the IBM Zurich Research Laboratory in Switzerland, working mainly on microcantilever devices for chemical AFM applications. At CNU, his research interests include smart cantilever devices, miniaturized energy harvester, smart structures & materials, and nanoscale transducers. He is a member of the technical program committee of IEEE Sensors Conference, Transducers, and Microprocesses and Nanotechnology Conference.